Mechanical Systems and Signal Processing 146 (2021) 107007

Contents lists available at ScienceDirect

Mechanical Systems and Signal Processing

journal homepage: www.elsevier.com/locate/ymssp

Modeling and experimental study of dynamic characteristics of the moment wheel assembly based on structural coupling

Mingyi Xia [a], Chao Qin [a], Xiaoming Wang [a], Zhenbang Xu [a,b,*]

[a] *CAS Key Laboratory of On-orbit Manufacturing and Integration for Space Optics System, Changchun Institute of Optics, Fine Mechanics and Physics, Chinese Academy of Sciences, Jilin, Changchun 130033, China*
[b] *Center of Materials Science and Optoelectronics Engineering, University of Chinese Academy of Sciences, Beijing 100049, China*

A R T I C L E   I N F O

Article history:
Received 19 November 2019
Received in revised form 10 March 2020
Accepted 25 May 2020
Available online xxxx

Keywords:
Moment wheel assembly
MWA
Microvibration
Parameter identification
Structural coupling

A B S T R A C T

The microvibration of the satellite moment wheel assembly (MWA) is an essential input for integrated simulation analysis of spacecraft microvibration, which forms the basis for spacecraft vibration suppression. Therefore, it is important to guarantee high-precision data from ground measurements of vibration sources for research into the stabilization accuracy of large space telescopes. In general, a coupled wheel-to-structure disturbance model is more representative of the real environment, and two aspects of the coupling need to be considered: coupling caused by insufficient MWA stiffness and coupling caused by the vibration source installation structure. Therefore, this paper presents the relevant work conducted on these two coupling aspects. First, this paper proposes the amplification factor coefficient, which considers structural coupling based on the classical vibration model of the MWA. The average error in this case could be within 5%. This approach could reduce the computational requirements without affecting the quality of the results. Additionally, as the mass of the MWA is greater and the disturbance output is more obvious. The structural coupling with the installation foundation is unavoidable. In this paper, the effects of installation stiffness on the disturbance measurements are analyzed based on the dynamic mass measurement method and quantitative impedance theory. Finally, based on the above theory, verification testing of the disturbance and transfer models of the MWA is performed and the test results are compared with the simulation results; it is shown that a level of accuracy within ±5% can be achieved.

1. Introduction

As the development of space exploration technology continues, increasing attention is been paid to microvibration in spacecraft [1–4]. Microvibration considerations are especially important in the development of China's large space telescope. The astronomical observation mode of this telescope requires long gaze and exposure times, its weight may exceed 15000 kg, and the diameter of the main mirror is 2 m. Additionally, the telescope's optical resolution is close to that of the Hubble Space Telescope (HST), and its field of vision is 300 times that of the HST. If the telescope is in orbit for 10 years, it will observe more than 40% of the sky area and approximately 17,500 square degrees. Because of its long focal lengths and

* Corresponding author at: CAS Key Laboratory of On-orbit Manufacturing and Integration for Space Optics System, Changchun Institute of Optics, Fine Mechanics and Physics, Chinese Academy of Sciences, Jilin, Changchun 130033, China.

E-mail address: xuzhenbang@ciomp.ac.cn (Z. Xu).

https://doi.org/10.1016/j.ymssp.2020.107007
0888-3270/

large scale, the spacecraft structure is more complex, leading to this telescope more sensitive to microvibration. To study the effects of microvibration on the telescope system, it will be necessary to study the disturbance mechanisms of the moving parts on the space telescope. The moment wheel assembly (MWA), which is one of the most widely used attitude control devices in high-resolution sensing satellites, is also the main disturbance source. As a typical high-speed rotating part, the MWA can provide the necessary control torque but can also produce disturbances that can then affect the line of sight (LOS). Therefore, it is of major importance to establish a simple and practical disturbance model of the MWA to enable implementation of corresponding isolation technology and control methods.

At present, the most commonly used space MWAs can be divided into two types: the symmetrical type and the cantilever type [5–8]. There is only a slight difference between these two configurations, which involves the radial translation and inplane rotation modes. In the symmetrical configuration, these two modes are independent, whereas the modes are coupled in the cantilever configuration. For application to the attitude adjustment mechanism of large space telescopes, the cantilever structure would generally be selected to obtain better performance and this structure is thus the main research focus of the work in this paper. Using this configuration, Bialke [9] provided a comprehensive description of the microvibration mechanism through experimental study and mathematical modeling of the MWA. Davis [10] first proposed a steady-state disturbance model of the reaction flywheel for the HST. Masterson and Miller [11,12] established an accurate dynamic disturbance model based on the steady-state disturbance model to predict the effects of vibration on a precision spacecraft telescope. They also established a disturbance model based on a data set to predict the vibration behavior of the HST's reaction wheel; the results indicated that the overall disturbance of the MWA was composed of irregular order harmonics with amplitudes that were proportional to the square of the rotor rotation speed. Liu and Maghami [13] of NASA fully considered the effects of noise on the disturbance characteristics. A semi-analytical model of the multi-dimensional disturbance output from the MWA was also established based on the harmonic and structural modes. This analytical model also considered the effects of harmonic disturbance, resonance amplification and noise on the MWA. After studying the disturbance characteristics of the MWA, Shankar Narayan and Nair [14] proposed that if the stiffness of the installation foundation was insufficient, the disturbance output of the MWA would then have a significant coupling effect with the installation structure when the rotor entered the working state; this would affect the observation accuracy of the satellite quite obviously. To resolve this type of coupling disturbance, it was necessary to study the disturbance transfer path of the satellite structure first and then understand how the disturbances of the moving parts could affect the camera imaging quality. The two most commonly used disturbance models for this purpose were the empirical model and the analytical model [15–18]. The empirical model assumed that the disturbance consisted of discrete sine waves with random phases, while the amplitude was directly proportional to the square of the rotor rotation speed. In addition, this model could express the disturbance variation trend effectively, but could not reflect the structural mode effect of the MWA on the disturbance characteristics. The analytical model included the internal elasticity effect of the flywheel, which could reflect the radial force and moment, but it could not explain the axial disturbance. In addition, many physical parameters were required to establish the analytical model, which was not convenient for engineering applications. In view of the shortcomings of both the empirical model and the analytical model, this paper proposes an improved MWA disturbance model. The main purpose of this work is to study the disturbance characteristics of the MWA and thus establish an accurate disturbance model by combining the theoretical analysis with experimental research.

In addition, most satellite structures are composed of honeycomb plates with low stiffness to reduce their weight. Therefore, the effect of structural coupling between the MWA and the installation foundation on the LOS cannot be ignored. However, a rigid installation environment has generally been used for the vibration and microvibration measurement methods during the actual measurement process (isolated measurements, with the MWA rigidly grounded on a multi-axis dynamic platform, e.g., a Kistler table) [19–22]. Because the measurement operation using this method was simple to perform and the data processing time was fast, it was able to predict the disturbance characteristics of a vibration source in the nonresonant region precisely. The China's large space telescope, is characterized by a high modal density, with thousands of modes within 8–300 Hz, and there are multiple coupling resonance peaks. During analysis of the dynamic characteristics of the internal vibration sources, the elasticity of the installation foundation also had to be considered [19,23,24]. To resolve this type of problem, many researchers carried out the relevant work with the aim of determining the dynamic mass of the source [25,26], but most of these works were based on analysis of a flywheel rotor under static conditions and without the gyroscopic effect. At the same time, the commonly used dynamic measurement platform could not be applied directly to coupling measurements because of size and weight limitations. Therefore, it was necessary to design special test equipment to perform the vibration source coupling tests. Additionally, Zhang [27] proposed a detailed scheme to establish a dynamic mass model of the MWA with the gyroscopic effect. Although the results obtained were relatively accurate, test implementation of this method was difficult and the method required large-scale calculations. Addari [15] performed a finite element analysis of the system and tests based on the hard-mounted configuration of the coupled dynamics between a cantilever configured MWA and its supporting structure. They also modified the microvibration disturbance model of the MWA when in the rotor motion state. Taniwaki and Ohkami [28] described an air floating vibration detection system that was subsequently adopted for analysis of retainer-induced disturbances of the reaction wheel [29]. In addition, the system could operate with a maximum frequency of 20 Hz, which allowed more attention to be paid to the low-frequency characteristics of inorbit vibration sources. There have been relatively few studies in this field to date, particularly for the microvibration coupling of large space telescopes; the existing methods still have a gap in terms of acquisition of the accurate vibration source input for full frequency range flexible coupling. In this paper, a coupling transfer model and a corresponding test method are applied based on the principle of mechanical impedance. When combined with the improved model of the momentum wheel, this approach can be applied to laboratory operations to ensure the measurement accuracy of MWA microvibration disturbances.

In accordance with the discussion above, vibration source disturbance and transfer models are established that combine their respective advantages and are then verified experimentally. Based on this process, the work in this paper proceeds as follows. In Section 2, based on the experiments and engineering experience, an improved model of the MWA is proposed to represent the flexible coupling of the internal structure and is then verified through experiments. In Section 3, the coupling transmission characteristics of the MWA are analyzed and the disturbance transfer model is then established based on impedance theory. In Section 4, the accuracy of the above models is verified experimentally, and Section 5 presents the conclusions of this paper.

2. Disturbance mechanism of momentum wheel

As shown in Fig. 1 [14], the cantilever MWA structure is mainly composed of a rotor, a shell, a motor and a bearing. The rotor provides the control force, which is mainly concentrated on the outer edge of the wheel. The main function of the shell is to provide a specific degree of vacuum; the motor is a DC motor, and the bearing is either a rolling bearing or a magnetic bearing.

The disturbance during operation mainly comes from two mechanisms: a) the active disturbance force, which is caused by rotor rotation and mainly includes the rotor imbalance and the disturbances of the rolling bearing and the motor [30]; b) the structural modal response, where the active disturbance force in the working state can lead to an internal structural response from the MWA due to its lack of stiffness, which then can form a disturbing force acting toward the outside. Fig. 2 shows the typical waterfall curve [11] and harmonic disturbance slice diagram of the MWA. The slice diagram describes the amplitude characteristics of the ith order harmonic. According to the disturbance classical model, the amplitude of harmonic increases proportionally with the square of the speed, but due to the structural coupling, it will fluctuate irregularly at different speeds. And the rocking mode is the rigid mode of the MWA, which represents both the forward and reverse precessions and forms a V-shaped curve, the radial translation is the disturbance that does not change with variations in the rotor speed and mainly comes from the structural elasticity. As these harmonic and structural modal frequency responses intersect, there will be an obvious amplification of the disturbance output. In general, the maximum disturbance of a satellite platform occurs at the harmonic and structural modal intersection.

2.1. Classical disturbance model of momentum wheel and identification

In the classical disturbance model of the MWA, if the disturbance force is composed of sine wave discrete harmonics related to the speed of the momentum wheel, the mathematical model can be expressed as follows:

$$m_k(t) = \sum_{i=1}^{n} C_i^k \Omega^2 \sin(2\pi h_i \Omega t + \varphi_i) \tag{1}$$

where $m_k(t)$ is the disturbance force or moment; i is the harmonic order; Ω is the rotational speed, h_i is the order coefficient of harmonic, which can represent the frequency multiple of disturbance; C is the amplitude of the ith order harmonic corresponding to $m_k(t)$; and φ_i is the phase.

To verify the accuracy of the model, the least squares method is used for fitting of C. Based on the model assumptions, the relationship between the disturbing force amplitude and the speed amplitude is as shown in the following equation for a specified harmonic number:

$$\tilde{d}_{ij} = K\Omega^2 \tag{2}$$

Here, $\tilde{d}_{ij}$ is the theoretical amplitude corresponding to the ith harmonic and the jth rotation speed, and K is a constant coefficient. The error between the measured value and the theoretical value is expressed as follows:

$$e_{ij} = d_{ij} - K\Omega^2 \tag{3}$$

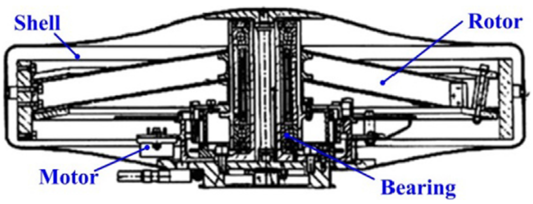

Fig. 1. Structure and schematic diagrams of momentum wheel.

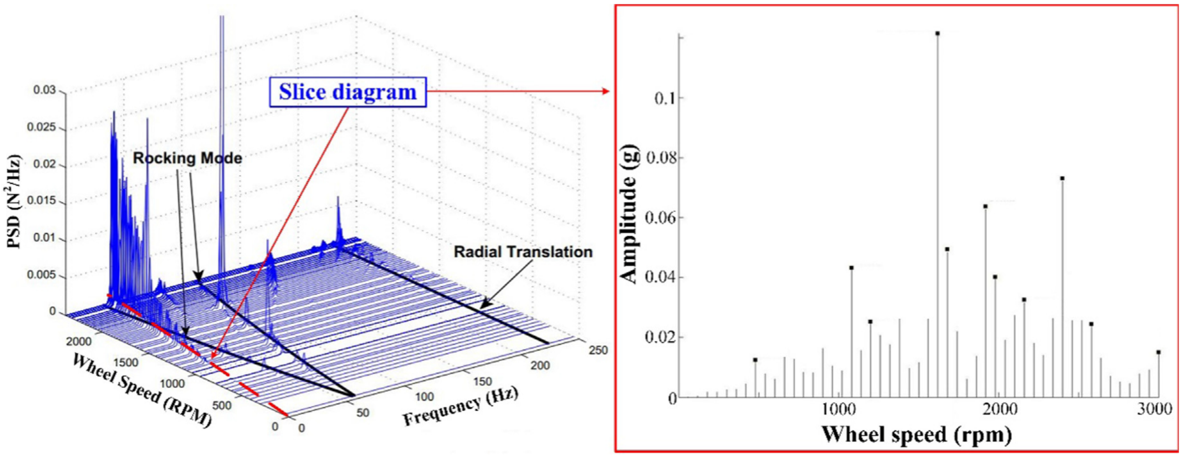

Fig. 2. Momentum wheel disturbance waterfall diagram and harmonic disturbance slice diagram.

where d_{ij} is the measured amplitude. The error expression is then squared and summed based on all the rotation speeds:

$$\sum_{j=1}^{m} {e_{ij}}^2 = \sum_{j=1}^{m} {d_{ij}}^2 - 2K\sum_{j=1}^{m} {\Omega_j}^2 d_{ij} + K^2\sum_{j=1}^{m} {\Omega_j}^4 \tag{4}$$

Here, C_i is defined as the value of K with the smallest squared error. The above equation is then used to derive K, and the result is shown as follows:

$$\frac{\partial}{\partial K} e_{ij}^2 = -2\sum_{j=1}^{m} \Omega_j^2 d_{ij} + 2K_i \sum_{j=1}^{m} \Omega_j^4 \tag{5}$$

If the above equation is equal to zero, and the expression for C_i can be obtained, then:

$$C_i = \frac{\sum_{q=1}^{n} d_{ij}^k \Omega_j^2}{\sum_{j=1}^{n} \Omega_j^4} \tag{6}$$

The model parameters must be identified via experiments. The test system used is shown in Fig. 3. The measured MWA is mounted on the load platform of the high-rigidity platform for six-dimensional force measurement to ensure that the stiffness of the installation structure does not affect the distribution of the vibration characteristics of the momentum wheel [31].

F_{lp}^k (k = 1,2,3,. . .6) is the output six-dimensional force signal, where l indicates the different speeds (ranging from 0 r/min to 3600 r/min, with data acquired once every 200 increments); p indicates the different time acquisition points when the sampling frequency is 2048 Hz and the length is 16 s; $\overline{F}_{lp}^{k}$ is the fast Fourier transform (FFT) of F_{lp}^k, where q is the discrete

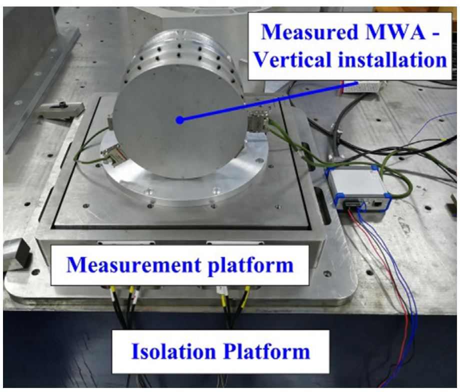

Fig. 3. Photograph of test system used to obtain the disturbance of the MWA.

frequency point, the frequency resolution is 0.0625 Hz, and the length is 1000 Hz. Let the amplitude of $\bar{F}_{lp}^{k}$ be plotted along the Z-axis, while the X and Y axes represent the rotation speed and frequency, respectively, and a waterfall curve can then be obtained, as shown in Fig. 4. In the resulting disturbance waterfall curve of the MWA, every order harmonic, V-shaped curve and fundamental response of the structure can be identified clearly. Using the above data and the least squares method, we can obtain the classical disturbance model of this MWA. The identification parameters for the first four orders of the harmonics are listed in Table 1.

2.2. Improved MWA disturbance model and its identification

The measured disturbance curve (Fig. 4) shows that the harmonics of each order are obviously amplified by the structural mode coupling, i.e., the structural coupling characteristics caused by the elastic structure, which cannot be described adequately using the classical model. For this reason, this paper proposes an improved disturbance model based on the experimental data:

$$m(t) = \sum_{i=1}^{n} \tilde{C}_i \cdot \beta_i \cdot \Omega^2 \sin(2\pi h_i \Omega t + \phi_i) \tag{7}$$

where $\tilde{C}_i$ is the amplitude of the ith harmonic of the improved model, with dimensions of N/Hz^2 or Nm/Hz^2, and $\beta_i(h_i\Omega)$ is the newly introduced amplification factor. The amplification factor is built based on the classical model of the MWA and the principle of modal superposition under the linear assumption. When the vibration source resonates with the structure, the relative motion transfer rate caused by the coupling can be obtained:

$$T_R = \frac{\bar{\omega}^2}{\sqrt{\left(1-\bar{\omega}^2\right)^2 + \left(2\xi\bar{\omega}\right)^2}} \tag{8}$$

where $\bar{\omega} = \omega/\omega_0$, ω_0 is the natural frequency of the structure, ξ is the modal damping ratio. By superimposing the resonance characteristics of each order harmonic and the structure of MWA, the coupling amplification factor for the wheel itself can be established, which is expressed as:

$$\beta_i = \beta_i(h_i\Omega) = \sum_{j=1}^{m} \frac{\alpha_j}{\sqrt{\left(1 - s_{ij}^2(\Omega)\right)^2 + \left(2\xi_{ij} s_{ij}(\Omega)\right)^2}}, \; s_{ij}(\Omega) = \frac{h_i\Omega}{\omega_j} \tag{9}$$

where m is the total number of natural frequencies of the structure; Because each order harmonic has different coupling characteristics with the structure, for some harmonics, they do not resonate with the structure, so in practice, $m(i)$ is the function of i, which should be identified; ω_j is the ith order natural frequency; ξ_{ij} is the modal damping ratio corresponding to each order of harmonics and modes; and α_j is the amplification factor at each natural frequency. The model considers the characteristics of the disturbances excited by the different mechanisms during coupling. A parametric model is proposed for the harmonic resonance that can improve the simulation accuracy of the output disturbance effectively under vibration source coupling conditions.

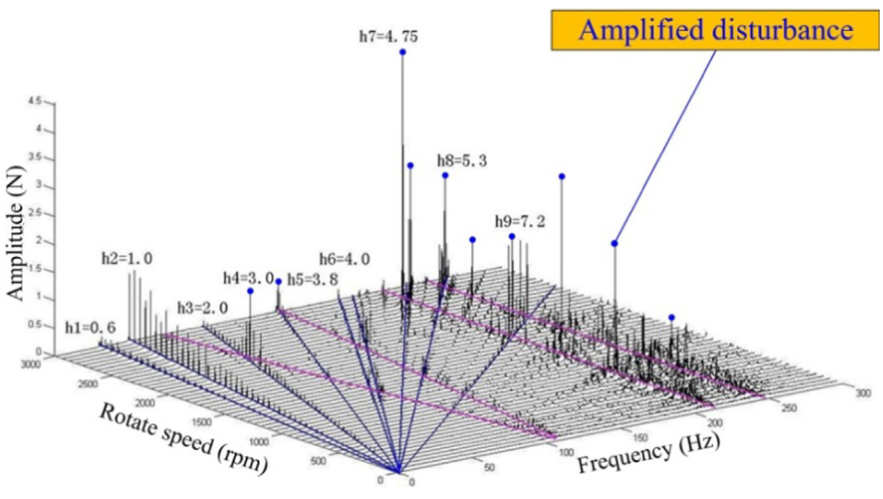

Fig. 4. Disturbance waterfall curve of F_x.

To identify these model parameters, we set $\alpha_j = 1$, then normalize the coefficient vector and thus obtain the following identification equation for the model:

$$\begin{bmatrix} m_i(\Omega_1) \\ m_i(\Omega_2) \\ \\ m_i(\Omega_p) \end{bmatrix} = \tilde{C}_i \cdot \begin{bmatrix} \Lambda_{i1}(\Omega_1) & \Lambda_{i2}(\Omega_1) & \cdots & \Lambda_{im}(\Omega_1) \\ \Lambda_{i1}(\Omega_2) & \Lambda_{i2}(\Omega_2) & \cdots & \Lambda_{im}(\Omega_2) \\ \vdots & \vdots & \ddots & \vdots \\ \Lambda_{i1}(\Omega_p) & \Lambda_{i2}(\Omega_p) & \cdots & \Lambda_{im}(\Omega_p) \end{bmatrix} \begin{bmatrix} \alpha_1 \\ \alpha_2 \\ \vdots \\ \alpha_m \end{bmatrix} \tag{10}$$

where p is the total number of speed measurement points, and $\Lambda_{ij}(\Omega) = \frac{\Omega^2}{\sqrt{\left(1-s_{ij}^2(\Omega)\right)^2 + \left(2\xi_{ij}s_{ij}(\Omega)\right)^2}}$.

Using the measured data, the slice d_{iq}^k is obtained for each harmonic. In this paper, the identification method for the single frequency mode is used for the estimation and the predicted values of the natural frequency $\omega_{ij}^{(0)}$ and the damping ratio $\xi_{ij}^{(0)}$ are obtained, where i denotes the harmonic order number and j denotes the modal order number. By taking the predicted values $\omega_{ij}^{(0)}$ and $\xi_{ij}^{(0)}$ as the initial values of ω_{ij} and ξ_{ij}, respectively, we can then obtain the first estimated value $\alpha_j^{(1)}$ of the linear parameter from the first iteration, and the variance $E^{(1)}$ can then be estimated for the first time. Generally, the preset precision μ for $E^{(1)}$ will not be satisfied, but by using the small variables $\Delta\omega_{ij}^{(0)}$ and $\Delta\xi_{ij}^{(0)}$, we can obtain the natural frequency and the damping ratio from the second iteration:

$$\omega_{ij}^{(1)} = \omega_{ij}^{(0)} + \Delta\omega_{ij}^{(0)}, \ \xi_{ij}^{(1)} = \xi_{ij}^{(0)} + \Delta\xi_{ij}^{(0)} \tag{11}$$

From Eq. (11), we can obtain the second estimates of the linear parameter $\alpha_j^{(2)}$ and the variance $E^{(2)}$. We then verify whether $E^{(2)}$ is less than or equal to μ; if not, $\omega_{ij}^{(1)}$ and $\xi_{ij}^{(1)}$ must be modified again until the condition $E \leqslant \mu$ is met, and then the linear parameter α_j and the nonlinear parameters ω_{ij} and ξ_{ij} will be used as the final estimated values. The parameter identification results for the improved model are presented in Table 2.

Table 1
0.1 Nm momentum wheel classical model parameters obtained from rigid measurement platform.

Harmonic Parameters		$C_i^k(\mu\mathrm{N/Hz^2})$			$C_i^k(\mu\mathrm{Nm/Hz^2})$		
i	h_i	F_x	F_y	F_z	M_x	M_y	M_z
1	0.6	33.28	31.25	28.56	6.89	7.59	0.25
2	1	77.26	99.68	33.65	4.69	10.26	4.58
3	2	29.63	26.39	11.23	18.56	36.65	12.36
4	3	18.58	25.68	26.36	8.88	21.56	0.88

Table 2
Identification results from improved model of 0.1 Nm MWA (first three orders of harmonics).

h_i	Parameters	F_x	F_y	F_z	M_x	M_y	M_z
0.6	α_1	33.28	31.25	11.53	6.89	7.59	0.25
1.0	α_1	28.21	18.56	11.26	38.25	5.69	0.66
	ω_1	66.97	62.56	28.56	62.15	33.71	26.73
	ξ_1	0.065	0.044	0.008	0.075	0.072	0.021
2.0	α_1	18.56	21.47	5.26	8.26	7.69	38.26
	ω_1	63.71	60.25	33.25	59.64	62.71	21.56
	ξ_1	0.009	0.003	0.003	0.026	0.013	0.485
	α_2	0.25	0.88	0.15	none	none	0.01
	ω_2	63.25	66.98	102.5	none	none	78.36
	ξ_2	0.036	0.005	0.188	none	none	0.031
3.0	α_1	8.78	18.26	7.55	6.25	3.66	0.08
	ω_1	63.25	67.92	78.56	95.36	97.52	83.58
	ξ_1	0.007	0.006	0.031	0.025	0.036	0.005
	α_2	0.58	0.36	0.78	0.61	0.82	0.98
	ω_2	83.26	88.25	111.2	160.2	177.2	101.2
	ξ_2	0.011	0.052	0.021	0.022	0.032	0.017
	α_3	0.44	0.15	0.74	none	none	0.95
	ω_3	175.23	166.0	175.2	none	none	178.3
	ξ_3	0.025	0.007	0.065	none	none	0.035

2.3. Fitting precision of disturbance model

Using the parameters identified via the two models above, the h_2 = 1, h_4 = 3, and h_8 = 5.3 (h_8 is not shown in Table 2) harmonics slice diagrams of F_x are calculated for fitting precision. However, the classical model does not involve structural coupling, in the identification process, only the order coefficient h_i and the amplitude C need to be identified. When coupling occurs near the sensitive frequency band, the model cannot improve the accuracy by optimizing the parameters. Therefore, in this paper the least square method is used for fitting quadric curve during establishing the classical model. The results are shown in Fig. 5 and Fig. 6.

For F_x, the harmonics of h_2 = 1 average fitting error of the improved model within the coupling frequency range is 4.71%. For the harmonics of h_4 = 3, the average fitting error is 0.91%.

For F_x, the harmonics of h_8 = 5.3 average fitting error of the improved model is 3.83%. Comparison of Fig. 5 and Fig. 6 shows that the improved model provides significantly higher fitting precision within the coupling frequency range. From the error statistics, the average error of the improved model over the entire measured frequency range can be within 5%. Simultaneously, because the basic assumptions are the same, the parameters of the improved model for the uncoupled frequency band are consistent with those of the classical model. As shown in Table 1 and Table 2, the amplitude parameter A of F_x for the 0.6× frequency harmonics has the same value of 33.28 μN/Hz^2 for two model types; additionally, for the classical model, C_i is 29.63 μN/Hz^2 when F_x is doubled, and is 26.39 μN/Hz^2 when F_y is doubled. The corresponding values from the improved model in the two cases above are 18.56 μN/Hz^2 and 21.47 μN/Hz^2, respectively. This is mainly because the classical model homogenizes the internal resonance energy of the MWA via C_i with respect to the entire measured frequency band, while the improved model quantifies the resonance effect of the formant using $\beta_i(h_i\Omega)$.

However, it should be noted that, as shown in Fig. 6, a large and uncontrollable error occurs near 1800 r/min. This error is due to an MWA design defect, which causes an unidentified mode to appear at approximately 30 Hz. This situation is often encountered in microvibration research; this type of mode, which includes the additional mode introduced by installation foundation, often brings reduced fitting precision obviously because of so many harmonics and their coupling parameters that is difficult to identify completely in most cases. Therefore, in the face of a complex installation environment, this paper

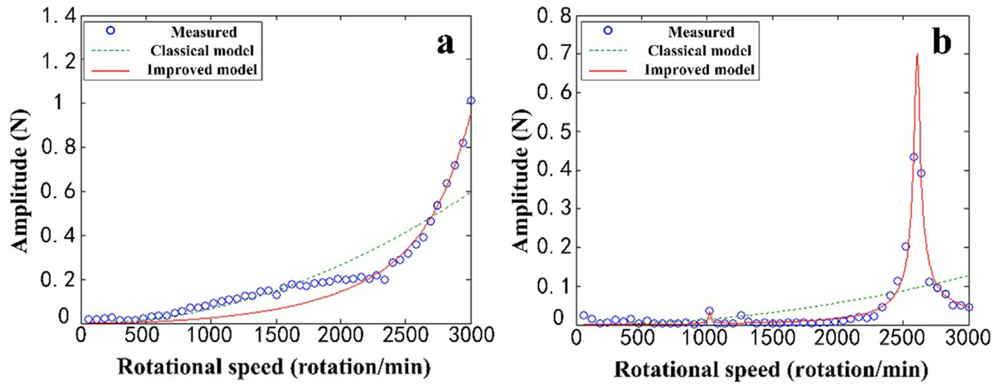

Fig. 5. Harmonics slice diagrams of F_x: (a) h_2 = 1; (b) h_4 = 3.

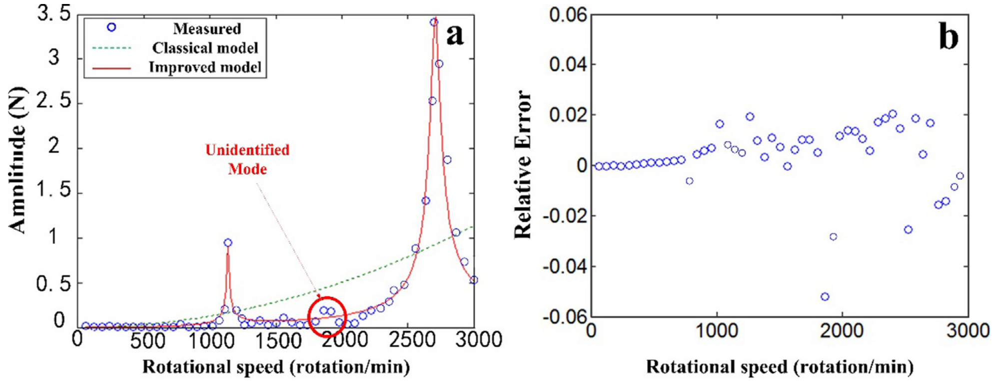

Fig. 6. Harmonics slice diagram and fitting error of F_x, (a) slice diagram of harmonics of h_8 = 5.3; (b) fitting relative error.

establishes a coupling transfer model based on the principle of mechanical impedance to compensate for the fitting precision of the disturbance model.

3. Establishment of coupled transformation model for vibration source disturbance

An improved disturbance model based on the MWA disturbance mechanism is established in this paper that can describe the disturbance force output of the MWA in the coupling state effectively. However, the scale of spacecraft is increasing, with China's large space telescope in particular expected to reach a mass of 15 t. In addition, the torque output index and the size of the internal MWA of this telescope will be significantly increased, while the coupling effects of the vibration sources and the installation foundation cannot be ignored. Therefore, this paper analyzes the disturbance transformation characteristics by considering structural coupling for the MWA based on both the modeling method and experimental methods.

3.1. MWA coupling transfer model

The disturbance in the working state of the flywheel is denoted by F_{wheel}. Because of the heavier mass of the large space telescope and the greater disturbance for the MWA, the acceleration response $\ddot{X}$ of the installation interface will result in the interaction force F being greater than the vibration source disturbance input. This relationship is illustrated in Fig. 7.

Here, F has the same amplitude and is acting in the opposite direction between the MWA and the installation interface; and the acceleration response $\ddot{X}$ under coupling conditions is acting in the same direction, i.e.:

$$F(\omega,\Omega) = Z_W(\omega,\Omega)W(\omega,\Omega) - Z_D(\omega,\Omega)\ddot{X}(\omega,\Omega) \tag{12}$$

where $\mathbf{Z}_D(\omega,\Omega)$ is the acceleration impedance matrix of the MWA, $\mathbf{W}(\omega,\Omega)$ is the MWA's "pure" disturbance force, equaling to $\mathbf{F}_{\text{wheel}}$, $\mathbf{Z}_W(\omega,\Omega)$ is the disturbance force transfer matrix between $\mathbf{W}(\omega,\Omega)$ and the elastic installation interface disturbance, $\mathbf{F}(\omega,\Omega)$ is the disturbance force of the installation interface, and $\ddot{X}(\omega,\Omega)$ is the acceleration response function of the installation interface, and they are all functions of the frequency ω and speed $\mathbf{\Omega}$.

At the installation interface of the MWA and the disturbance measurement platform, the following relationship exists:

$$Z_P(\omega)\ddot{X}(\omega,\Omega) = F(\omega,\Omega) \tag{13}$$

where $\mathbf{Z}_P$ is the acceleration impedance matrix of the installation interface.

From Eq. (13), we obtain:

$$\ddot{X}(\omega,\Omega) = [Z_P(\omega)]^{-1}F(\omega,\Omega) \tag{14}$$

Using Eq. (14) as a basis, the disturbance translation model given in Eq. (13) can be expressed as:

$$F(\omega,\Omega) = \left[I + Z_D(\omega,\Omega)[Z_P(\omega)]^{-1}\right]^{-1}Z_W(\omega,\Omega)W(\omega,\Omega) \tag{15}$$

$$F(\omega,\Omega) = Z_W(\omega,\Omega)W(\omega,\Omega) - Z_D(\omega,\Omega)[Z_P(\omega)]^{-1}F(\omega,\Omega) \tag{16}$$

Because the "pure" disturbance force and the torque of the MWA cannot be measured directly, it is necessary to simplify the model to ensure the feasibility of the test. It can be seen from Eq. (12) that if the acceleration$\ddot{X}(\omega,\Omega)$of the installation interface is 0, then the disturbance force and the torque of the installation interface can be regarded as a substitute for $\mathbf{Z}_W(\omega,\mathbf{\Omega})\mathbf{W}(\omega,\Omega)$ in Eq. (16). Additionally, because the natural frequency of the rigid measurement platform is much higher than the natural frequency of the MWA, the acceleration $\ddot{X}(\omega,\Omega)$ of the interface can be considered to be 0, so $\mathbf{Z}_W(\omega,\Omega)\mathbf{W}(\omega,\Omega)$ can be approximately equal to $\mathbf{F}|_W(\omega,\Omega)$, which is the disturbance of the MWA obtained using the rigid measurement platform, i.e.:

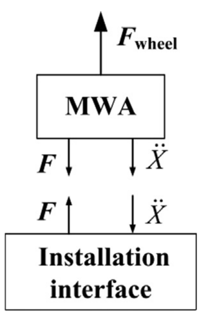

Fig. 7. Interaction between MWA and installation interface.

$$F(\omega,\Omega) = [I + Z_D(\omega,\Omega)[Z_P(\omega)]^{-1}]^{-1} F|_W(\omega,\Omega) \tag{17}$$

The acceleration admittance is easier to measure during the microvibration test and Eq. (17) can then be converted into an equation based on the acceleration admittance matrix, i.e., $\mathbf{H}_D(\omega,\Omega) = [\mathbf{Z}_D(\omega,\Omega)]^{-1}$, $\mathbf{H}_P(\omega) = [\mathbf{Z}_P(\omega)]^{-1}$; Eq. (17) is then transformed into Eq. (18) as follows:

$$F(\omega,\Omega) = \{I + [H_D(\omega,\Omega)]^{-1} H_P(\omega)\}^{-1} F|_W(\omega,\Omega) = G_f(\omega,\Omega) F|_W(\omega,\Omega) \tag{18}$$

where $\mathbf{G}_f(\omega,\Omega)$={$\mathbf{I}$ + [$\mathbf{H}_D(\omega,\Omega)]^{-1}\mathbf{H}_P(\omega)\}^{-1}$ is the coupling disturbance matrix. $\mathbf{F}(\omega,\Omega)$ and $\mathbf{F}|_W(\omega,\Omega)$ are the dynamics disturbance matrices of the MWA on the target elastic and rigid measurement platforms, respectively, including the three disturbance forces and the three disturbance moments, which are 6×1 matrices; $\mathbf{H}_D(\omega,\Omega)$ and $\mathbf{H}_P(\omega)$ are the acceleration admittance matrix of the MWA itself and the acceleration admittance matrix of the installation structure, respectively, and are both 6×6 matrices.

$$F_i(\omega,\Omega) = \left[1/\left(1 + \frac{H_{Pi}(\omega)}{H_{Di}(\omega,\Omega)}\right)\right] \times F_i|_W(\omega,\Omega),\ (i = 1,2,3,4,5,6) \tag{19}$$

3.2. Parameter identification of acceleration admittance matrix of MWA

To obtain the acceleration admittance matrix $\mathbf{H}_{Di}$ (i = 1,2,3) in Eq. (19), the acceleration impedance of the MWA can be obtained from Eq. (12):

$$Z_D(\omega,\Omega) = (Z_W(\omega,\Omega)W(\omega,\Omega) - F(\omega,\Omega))\left[\ddot{X}(\omega,\Omega)\right]^{-1} \tag{20}$$

Additionally, because $\mathbf{Z}_W(\omega,\Omega)\mathbf{W}(\omega,\Omega)$ can be replaced with $\mathbf{F}|_W(\omega,\Omega)$, Eq. (20) can be expressed as:

$$Z_D(\omega,\Omega) = (F|_W(\omega,\Omega) - F(\omega,\Omega))\left[\ddot{X}(\omega,\Omega)\right]^{-1} \tag{21}$$

Based on the relationship between the acceleration impedance and the admittance, the above equation can be expressed as:

$$H_D(\omega,\Omega) = [Z_D(\omega,\Omega)]^{-1} = \left\{(F|_W(\omega,\Omega) - F(\omega,\Omega))\left[\ddot{X}(\omega,\Omega)\right]^{-1}\right\}^{-1} \tag{22}$$

where given that the three translational degrees of freedom of the MWA are decoupled from each other and $\mathbf{H}_D(\omega,\Omega)$ is thus a diagonal matrix, the above equation can be simplified to a single degree of freedom only for the translation form:

$$H_{Di}(\omega) = \frac{1}{(F_i|_W(\omega) - F_i(\omega))/\ddot{X}_i(\omega)},\ (i = 1,2,3) \tag{23}$$

To obtain a smooth acceleration admittance function, the disturbance $\mathbf{F}_i|_W$ of the MWA on the rigid measurement platform, the disturbance $\mathbf{F}_i$ that acts on the elastic installation structure for the MWA, and the acceleration at the installation interface can be measured during testing and converted into the power spectrum and admittance function. Additionally, the radial disturbance mode frequency ω_{radial} and the axial translational mode ω_{axial} of the MWA can be identified using the rational polynomial identification method for modal parameters.

3.3. Experiment and simulation verification

3.3.1. Experimental system

To verify the simulation results from the different disturbance transformation models, the disturbance of the MWA is measured under various stiffness conditions using the eight-component force measurement platform [31]. Furthermore, the MWA is in the vertical mounting and the sampling frequency of the data acquisition system (accuracy: ±0.1 dB; 652u-24 bit, IOTech, Norton, MA, USA) is set at 2048 Hz. During the acquisition process, the data are subjected to preprocessing, which includes elimination of zero drift, elimination of interference and improvement of the signal-to-noise ratio (SNR) [32,33].

Fig. 8 shows the experimental diagram of the MWA on the rigid and flexible installation foundations, which are used to simulate the real installation conditions of a space-based scope. Based on these experimental systems, the MWA disturbance force matrices $\mathbf{F}(\omega,\Omega)$ and $\mathbf{F}|_W(\omega,\Omega)$ can be obtained with the flexible and rigid constraints; according to Eq. (22) and Eq. (23), the acceleration admittance matrix $\mathbf{H}_D(\omega,\Omega)$ of MWA and the acceleration admittance matrix $\mathbf{H}_P(\omega)$ of the installation structure are obtained based on the six-dimensional disturbance force and acceleration matrix of the installation interface. In order to obtain the 6-dimensional acceleration data, as shown in Fig. 9, a measurement method is designed through three 3-axial acceleration sensors (a1, a2, a3) in a 120° distribution on the installation interface. The acceleration sensors (b1, b2) at the center and edges of the wheel can be used to classify and analyze the internal disturbance mechanism of MWA.

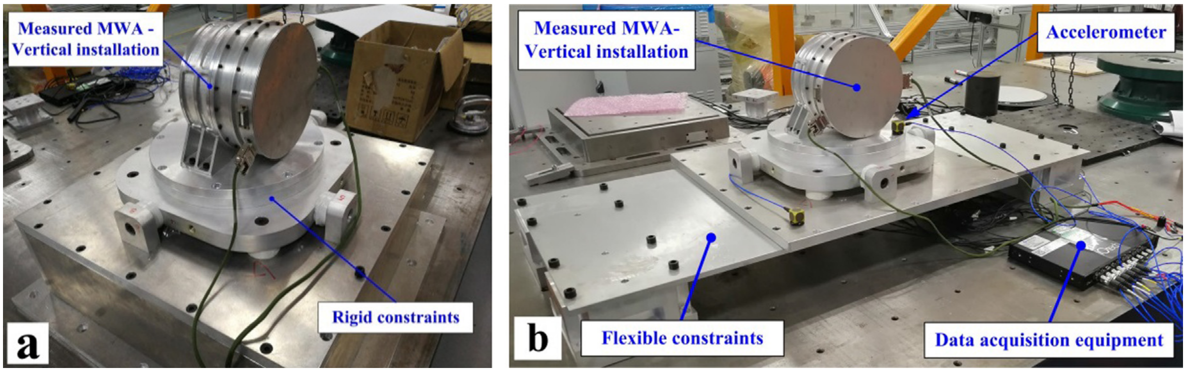

Fig. 8. Photograph of the MWA disturbance experiment: (a) rigid installation; (b) flexible installation.

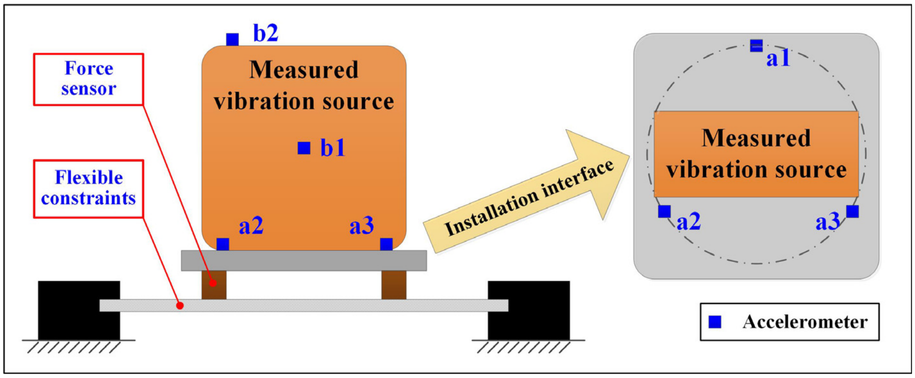

Fig. 9. Schematic showing the working principle of experiment with flexible installation.

First, the inherent properties of the elastic platform are tested. As shown in Fig. 10, the basic system frequency is 25.72 Hz, based on flexible installation of the MWA (static state). Then, the six-dimensional dynamic characteristics distribution of the MWA is tested under the different installation foundation stiffness conditions. The experimental results for F_x are shown in Fig. 11 and Fig. 12.

As shown in the experimental results above, the natural frequency of the MWA will shift because of the coupling relationship between the inherent characteristics of the MWA and those of the flexible foundation. The sway mode disturbance will obviously be weakened. In addition, the reverse precession and forward precession modes cannot be identified effectively. The disturbance characteristic distributions of the MWA at the rotation speed of 2100 r/min on the two measurement platforms are presented in Table 3.

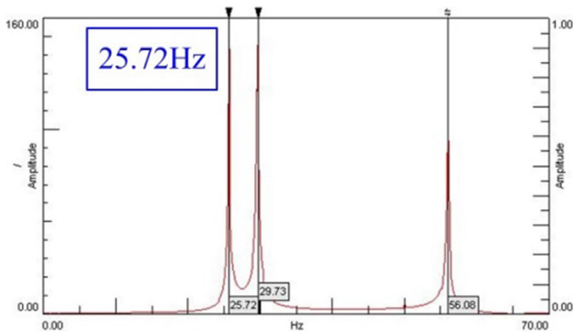

Fig. 10. Natural frequency of MWA structure based on flexible installation.

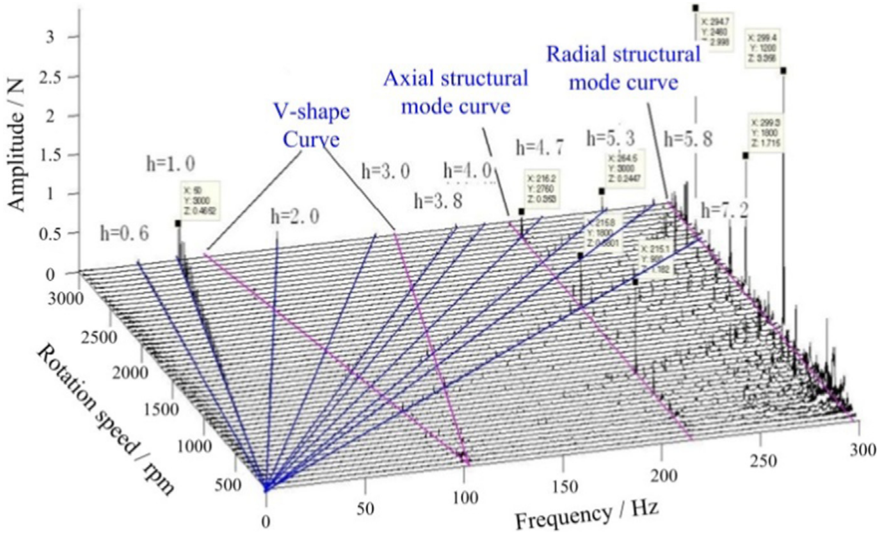

Fig. 11. F_x disturbance waterfall under rigid installation conditions.

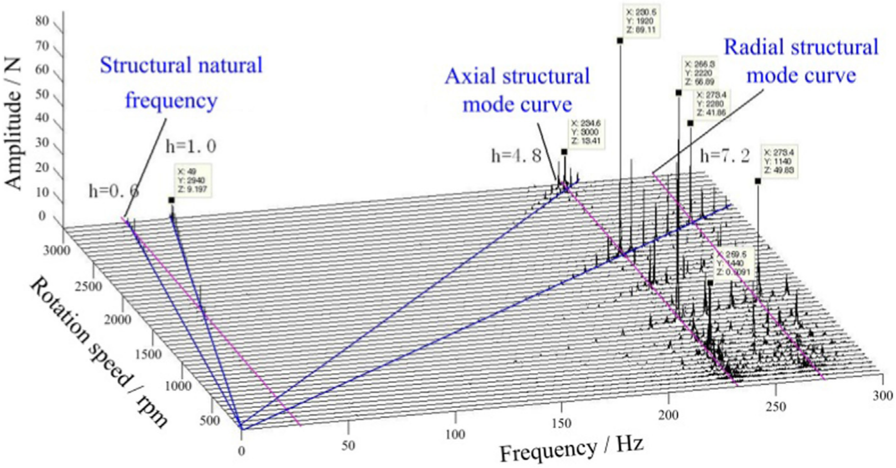

Fig. 12. F_x disturbance waterfall under flexible installation conditions.

Table 3
Disturbance frequency characteristics of momentum wheel on two experimental platforms (Hz).

Disturbance frequency	Forward precession	Reverse precession	Axial translational	Radial translational
Rigid installation	76	140	212	265
Flexible installation	–	–	230	273

3.3.2. Parameter identification and verification of the coupling transfer model

Based on the experimental data given above, m_1 is introduced as the mass of the external structure, m_2 represents the rotor mass, and the original displacement admittance of the MWA in its shell is shown as:

$$H_i = -\frac{1}{\omega^2(m_1 + m_2)} \frac{(1 - \bar{\omega}_{Ai}^2) + j2\xi_{Ai}\bar{\omega}_{Ai}}{(1 - \bar{\omega}_{Ri}^2) + j2\xi_{Ri}\bar{\omega}_{Ri}} \tag{24}$$

where $\bar{\omega}_{Ai} = \omega/\omega_{Ai}$, $\bar{\omega}_{Ri} = \omega/\omega_{Ri}$, and ω_{Ai} are the antiresonance frequencies of the two degrees of freedom system; ω_{Ri} is the resonance frequency; and ξ_{Ai} and ξ_{Ri} are the antiresonant damping and the resonant damping, respectively. Additionally, it is

Table 4
Comparison of the experimental and identification results for the modal parameters.

Modal parameters	ω_{axial} (Hz)	ω_{radial} (Hz)	ξ_{axial} (%)	ξ_{radial}(%)
Experimental results	214.6	268.7		
Identification results	211.2	266.3	2.1	1.6
Relative error (%)	1.58	0.89		

convenient to measure the acceleration admittance, and the relationship between the displacement admittance and the acceleration admittance is given as follows:

$$H_{Di} = H_i(-\omega^2) \tag{25}$$

Therefore, the original acceleration admittance of the MWA at its shell is given as follows:

$$H_{Di} = \frac{1}{m_1 + m_2} \frac{(1 - \bar{\omega}_{Ai}^2) + j2\xi_{Ai}\bar{\omega}_{Ai}}{(1 - \bar{\omega}_{Ri}^2) + j2\xi_{Ri}\bar{\omega}_{Ri}} \tag{26}$$

The shell mass of the momentum wheel m_1 = 2.5 kg, and the rotor mass m_2 = 7.5 kg. In this paper, the identification method for rational polynomial modal parameters is used to identify the modal parameters of the MWA disturbance force during stable rotation. The initial iteration values are given as: ω_{axial} = 220 Hz, ω_{radial} = 260 Hz, ξ_{axial} = 2%, and ξ_{radial} = 2%. The iterative process is skipped and the modal parameters of ω_{axial} = 211.2 Hz and ω_{radial} = 266.3 Hz are obtained by identification. A comparison of the experimental and identification results for the modal parameters is shown in Table 4, and the relative error is shown to be within 2%.

The frequency response characteristics obtained for axial translation and radial translation of the MWA and the frequency response function (FRF) of the flexible installation can be substituted into Eq. (19), which can then be used to predict the response of the MWA to the six-dimensional disturbance force acting on the flexible installation. Furthermore, a comparison of the predicted results with the experimental results measured under real installation conditions (where the random noise is ignored) is shown in Fig. 13.

As shown in Fig. 13, the predicted results reflect the disturbance frequency distribution of the MWA accurately under the different installation conditions. In addition, the natural frequency information measured using the rigid platform is not included in the prediction results because the decoupling effect is obvious. In particular, the prediction accuracy of

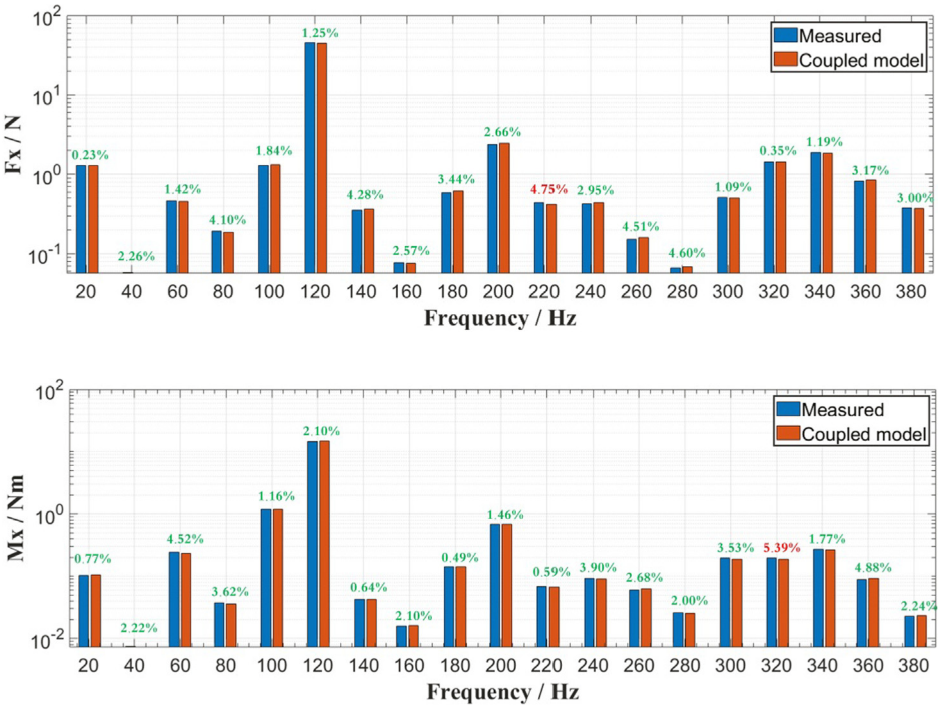

Fig. 13. Comparison of experimental and predicted results: (a) F_y (b) M_x.

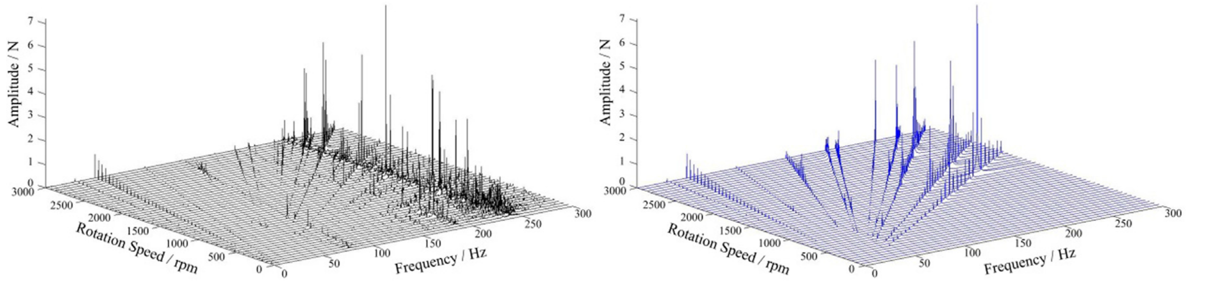

Fig. 14. Comparison of measured waterfall diagram and simulated diagram of the disturbance force F_x.

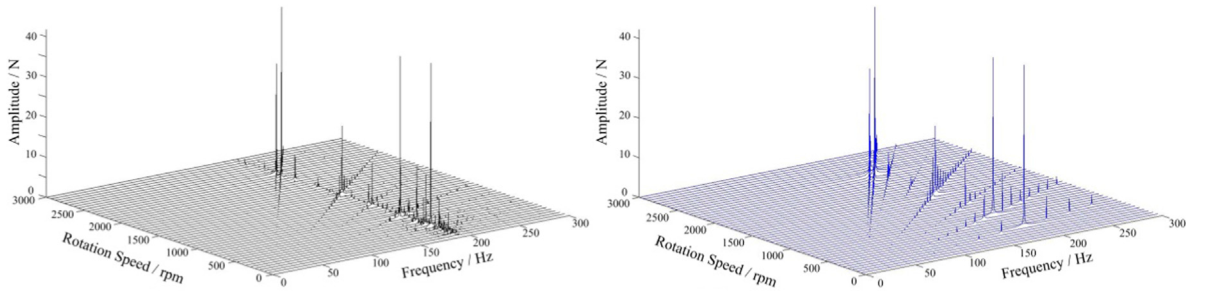

Fig. 15. Measured waterfall diagram and simulated diagram for disturbance force F_z.

the disturbance moment is improved, the prediction error for the overall six-dimensional force can be maintained at under 10% within the working frequency range of the large space telescope (8–300 Hz), and the relative error is mostly less than 5%

4. Experimental verification of integration model

Based on the improved disturbance model and the coupling transfer model of the MWA, the simulation results are a combination of the improved disturbance model and the coupling transfer model, which are both verified experimentally. The experimental results are the disturbance force data from the measured MWA on the simulated flexible installation foundation (Fig. 8). Using the simulated and experimental results, waterfall diagrams were generated for the six-dimensional disturbance force, which can indicate the fitting accuracy directly, as shown in Fig. 14 and Fig. 15. Where the measured waterfall diagram contains random noise; and in the simulated diagram, no Gaussian white noise is introduced, which has a low influence on the structural coupling for this MWA (the effect of noise on imaging quality with RMS is less than 10%). Therefore, only the simulation results that describe the structural coupling effects of line spectrum frequency are shown. However, for future ultra-high-precision telescopes, which will have a higher modal density, the stability requirements are more strict, and the effect of noise will be also more prominent, therefore, the characteristics of random vibration of MWA will be a considerable topic in future research.

Fig. 14 shows a comparison of the measured waterfall diagram and the simulation diagram for the same disturbance force F_x. The relative error of the model can be obtained by comparing the data of the harmonics of each order within the working frequency band, as shown in Table 5. The average relative error of F_x from the simulations is ε = 3.43%.

In addition, the simulated (first nine orders) and experimental results for F_z can also be obtained, as shown in Fig. 15.

From Fig. 15 and Table 6, the average error of the F_z modeling simulation in the working frequency band is ε = 3.56%. Based on the statistics of the disturbance force in the other directions, the integration model fitting accuracy for the six-dimensional force is within 5%.

Table 5
Fitting error of disturbance force F_x at each frequency doubling event.

h_i	0.6	1	2	3	3.8	4	4.8	5.3	7.2
Relative error /%	1.24	2.31	2.56	1.21	2.14	4.25	4.68	4.21	3.25

Table 6
Fitting errors of disturbance force F_z at each frequency doubling.

h_i	0.6	4.69	4.82	5.21	6.02	7.2	9.62	13.8	27.47
Relative error /%	1.45	3.56	1.13	7.46	4.50	0.94	1.14	0.25	0.99

5. Conclusions

In this paper, based on an empirical model, an improved dynamic disturbance model of the cantilever MWA is proposed that reflects the structural coupling effect of the MWA disturbance by introducing the amplification coefficient. The precision of the MWA disturbance model has been improved and the average fitting error is within 5% across the entire test frequency range. By considering the real installation foundation, this paper establishes a coupling transfer model based on impedance theory. Then, the rational polynomial identification method is used to identify the modal parameters of the MWA experimentally based on the rigid and flexible installation measurement platforms. The integration of the disturbance and transfer models is also verified experimentally. The error between the experimental results and those from the model is generally less than 5% (in the 8–300 Hz range).

Funding

This work was supported by the National Natural Science Foundation of China (NO. 11672290, NO. 11972343, NO. 91848202) and Funded and Supported by National Key R&D Program of China (NO. 2016YFE0205000).

CRediT authorship contribution statement

Mingyi Xia: Writing - original draft, Investigation, Methodology, Validation. **Chao Qin**: Validation, Visualization. **Xiaoming Wang**: Writing - review & editing. **Zhenbang Xu**: Conceptualization, Funding acquisition.

Declaration of Competing Interest

The authors declare that they have no known competing financial interests or personal relationships that could have appeared to influence the work reported in this paper.

References

[1] C. Liu, X. Jing, S. Daley, F. Li, Recent advances in micro-vibration isolation, Mech. Syst. Signal Process. 56 (2015) 55–80.
[2] A. Stabile, G.S. Aglietti, G. Richardson, G. Smet, Design and verification of a negative resistance electromagnetic shunt damper for spacecraft micro-vibration, J. Sound Vibr. 386 (2017) 38–49.
[3] O.L. de Weck, D.W. Miller, H. Guiterrez, Structural dynamics and control for ngst - a preliminary study, in: Proceedings of the 34th Lige International Astrophysics Colloquium, Lige, Belgium, 1998.
[4] ECSS-E-HB-32-26A Spacecraft Mechanical Loads Analysis Handbook, ESA Requirements and Standards Division, 2013.
[5] H. Wang, Q. Han, D. Zhou, Nonlinear dynamic modeling of rotor system supported by angular contact ball bearings, Mech. Syst. Signal Process. 85 (2017) 16–40.
[6] L. Li, L. Tan, L. Kong, D. Wang, H. Yang, The influence of flywheel micro vibration on space camera and vibration suppression, Mech. Syst. Signal Process. 100 (2018) 360–370, https://doi.org/10.1016/j.ymssp.2017.07.029.
[7] H. Wang, Q. Han, R. Luo, T. Qing, Dynamic modeling of moment wheel assemblies with nonlinear rolling bearing supports, J. Sound Vibr. 406 (2017) 124–145.
[8] B.J. Kawak, Development of a low-cost, low micro-vibration CMG for small agile satellite applications, Acta. Astronaut. 131 (2017) 113–122.
[9] B. Bialke, Microvibration disturbance fundamentals for rotating mechanisms, in: Proceedings of the 34th Annual Guidance and Control Conference, Breckenridge, CO, 2011.
[10] L.P. Davis, J.F. Wilson, R.E. Jewell, J.J. Roden, Hubble space telescope reaction wheel assembly vibration isolation system, NASA Marshall Space Flight Center, Huntsville, Alabama, 1986, 9.
[11] L.P. Davis, J.F. Wilson, R.E. Jewell, J.J. Roden, Hubble space telescope reaction wheel assembly vibration isolation system, NASA Marshall Space Flight Center, Huntsville, Alabama, 1986, 9.
[12] R.A. Masterson, D.W. Miller, R.L. Grogan, Development and validation of reaction wheel disturbance models: empirical model, J. Sound Vibr. 249 (3) (2002) 575–598, https://doi.org/10.1006/jsvi.2001.3868.
[13] K.C. Liu, P. Maghami, C. Blaurock, Reaction wheel disturbance modeling, jitter analysis, and validation tests for solar dynamics observatory, in: AIAA Guidance, Navigation and Control Conference and Exhibit, Honolulu, Hawaii, 2008.
[14] S.S. Narayan, P.S. Nair, A. Ghosal, Dynamic interaction of rotating momentum wheels with spacecraft elements, J. Sound Vibr. 315 (4–5) (2008) 970–984, https://doi.org/10.1016/j.jsv.2008.02.020.
[15] D. Addari, G.S. Aglietti, M. Remedia, Experimental and numerical investigation of coupled microvibration dynamics for satellite reaction wheels, J. Sound Vibr. 386 (2017) 225–241, https://doi.org/10.1016/j.jsv.2016.10.003.
[16] Z. Zhang, G. Aglietti, W. Ren, Microvibration model development and validation of a cantilevered reaction wheel assembly, Appl. Mech. Mater. 226–228 (2012) 133–137, https://doi.org/10.4028/www.scientific.net/AMM.226-228.133.
[17] I. Basdogan, L.M. Elias, F. Dekens, L. Sievers, Predicting the optical performance of the space interferometry mission using a modeling, testing, and validation methodology, J. Vibr Acoust 129 (2) (2007) 148–157.
[18] L.M. Elias, D.W. Miller, A coupled disturbance analysis method using dynamic mass measurement techniques, in: Proceedings of the 43rd AIAA/ASME/ASCE/AHS/ASC Structures, Structural Dynamics, and Materials Conference, Denver, Colorado, 2002.

[19] T. Wacker, L. Weimer, K. Eckert, Goce platform micro-vibration verification by test and analysis, in: European Conference on Spacecraft Structures, Materials & Mechanical Testing, Noordwijk, The Netherlands, 2005.
[20] Z. Zhang, G. Aglietti, Microvibration modelling and testing of a satellite reaction wheel, in: Proceedings of the European Conference of Mechanical Engineering (ECME'11), Puerto De La Cruz, Tenerife, 2011.
[21] X. Sun, B. Yang, A new methodology for developing flexure-hinged displacement amplifiers with micro-vibration suppression for a giant magnetostrictive micro drive system, Sensor. Actuat. A-Phys. 263 (2017) 30–43.
[22] Z. Feng, Y. Cui, X. Yang, J. Qin, Micro-vibration issues in integrated design of high resolution optical remote sensing satellites, in: Proceedings of 3rd International Symposium of Space Optical Instruments and Applications, Springer, Cham, 2017.
[23] L.M. Elias, F.G. Dekens, I. Basdogan, L.A. Sievers, T. Neville, A methodology for modeling the mechanical interaction between a reaction wheel and a flexible structure, in: Interferometry in Space, Waikoloa, HI, USA, 2003.
[24] E. Koekkoek, P. Gungo, R. Bureo Dacal, A realistic approach in the prediction of the aces micro-gravity environment, in: Proceedings of European Conference on Spacecraft Structures, Materials & Mechanical Testing, Noordwijk, The Netherlands, 2005.
[25] Z. Zhang, W. Ren, G. Aglietti, Coupled disturbance modelling and validation of a reaction wheel model, in: European Conference on Spacecraft Structures, Materials & Environmental Testing, The Netherlands, Noordwijk, 2012.
[26] Y. Zhao, P. Zhang, W. Cheng, Measurement and study of disturbance characteristics of reaction wheel assembly, J. Exp. Mech. 24 (6) (2009) 532–538.
[27] Z. Zhang, G.S. Aglietti, W. Ren, Coupled microvibration analysis of a reaction wheel assembly including gyroscopic effects in its accelerance, J. Sound Vibr. 332 (22) (2013) 5748–5765, https://doi.org/10.1016/j.jsv.2013.06.011.
[28] S. Taniwaki, Y. Ohkami, Experimental and numerical analysis of reaction wheel disturbances, JSME Int. J. Ser. C Mech. Syst., Mach. Elements Manuf. (46 (2), 2003,) 519–526, https://doi.org/10.1299/jsmec.46.519.
[29] S. Taniwaki, M. Kudo, M. Sato, Y. Ohkami, Analysis of retainer induced disturbances of reaction wheel, J. Syst. Des. Dyn. 1 (2) (2007) 307–317, https://doi.org/10.1299/jsdd.1.307.
[30] H. Wang, Q. Han, D. Zhou, Output torque modeling of control moment gyros considering rolling element bearing induced disturbances, Mech. Syst. Signal Process. 115 (2019) 188–212.
[31] M. Xia, Z. Xu, K. Han, Q. Huo, A. Li, Dynamic disturbance force measurement platform for large moving device in spacecraft, J. Sound Vibr. 447 (2019) 61–77, https://doi.org/10.1016/j.jsv.2019.01.053.
[32] Y.J. Li, J. Zhang, Z.Y. Jia, M. Qian, H.G. Li, Research on force-sensing element's spatial arrangement of piezoelectric six-component force/torque sensor, Mech. Syst. Signal Process. 23 (8) (2009) 2687–2698, https://doi.org/10.1016/j.ymssp.2009.05.014.
[33] Y.J. Li, G.C. Wang, J. Zhang, Z.Y. Jia, Dynamic characteristics of piezoelectric six-dimensional heavy force/moment sensor for large-load robotic manipulator, Measurement 45 (5) (2012) 1114–1125, https://doi.org/10.1016/j.measurement.2012.01.028.